Doolan, Jack, Alesbrook, L.S., Baker, Karen, Brown, I.R., Williams, George T., Hilton, Kira L.F., Tabata, Makoto, Wozniakiewicz, Penelope J., Hiscock, Jennifer R. and Goult, Benjamin T (2023) *Next-generation protein-based materials capture and preserve projectiles from supersonic impacts.* Nature nanotechnology, 18 (7). pp. 1060-1066. ISSN 1748-3387.

Kent Academic Repository

Doolan, Jack, Alesbrook, L.S., Baker, Karen, Brown, I.R., Williams, George T., Hilton, Kira L.F., Tabata, Makoto, Wozniakiewicz, Penelope J., Hiscock, Jennifer R. and Goult, Benjamin T (2022) *Next generation protein-based materials capture and preserve projectiles from supersonic impacts.* **Nature nanotechnology . ISSN 1748-3387. (In press)**

Next generation protein-based materials capture and preserve projectiles from supersonic impacts

Jack A. Doolan[1], Luke S. Alesbrook[2], Karen B. Baker[1], Ian R. Brown[1], George T. Williams[2,3], Kira L. F. Hilton[2], Makoto Tabata[4], Penelope J. Wozniakiewicz[5], Jennifer R. Hiscock[2]* and Benjamin T. Goult[1]*

[1]School of Biosciences, University of Kent, Canterbury, UK
[2]School of Chemistry and Forensic Science, University of Kent, Canterbury, UK
[3]Current address - Department of Chemistry, University of Southampton, Southampton, UK
[4]Department of Physics, Chiba University, Chiba, Japan
[5]School of Physics and Astronomy, University of Kent, Canterbury, UK

*To whom correspondence should be addressed, also denotes equal scientific input and joint authorship status. Email: B.T.Goult@kent.ac.uk (Professor Ben Goult) and J.R.Hiscock@kent.ac.uk (Professor Jen Hiscock).

Abstract

Extreme energy dissipating materials are essential for a range of applications. The military and police force require ballistic armour to ensure the safety of their personnel, while the aerospace industry requires materials that enable the capture, preservation and study of hypervelocity projectiles. However, current industry standards display at least one inherent limitation, such as weight, breathability, stiffness, durability and failure to preserve captured projectiles. To resolve these limitations we have turned to nature, utilising proteins that have evolved over millennia to enable effective energy dissipation. Specifically, a recombinant form of the mechanosensitive protein talin was incorporated into a monomeric unit and crosslinked, resulting in the production of the first reported example of a talin shock absorbing material (TSAM). When subjected to 1.5 km/s supersonic shots, TSAMs were shown not only to absorb the impact, but to capture/preserve the projectile.
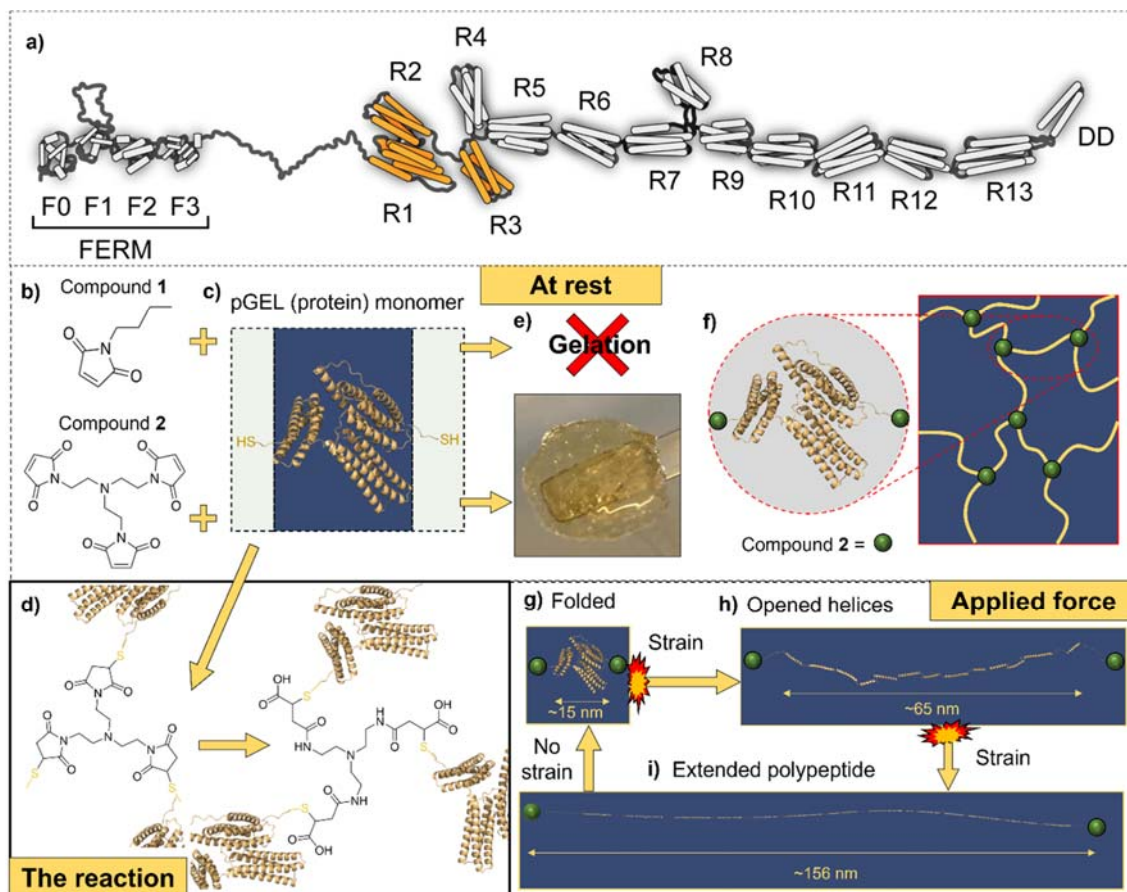
Main

When impacted by a projectile, a material is exposed to a variety of phenomena simultaneously. To survive the impact a material must contend with wave propagation (elastic, shock and plastic), fragmentation, perforation and spallation[1]. Thus, installing a mechanism within a material to enable effective energy dissipation is essential for multiple applications[2-4]. Body armour is commonly used by military and civilian forces to protect the wearer against penetration from projectiles, such as bullets or shrapnel[4]. Frequently, this armour consists of a multi-layered system, commonly a ceramic face backed by a fibre-reinforced composite[5]. This multi-layered design enables the hard brittle ceramic to destroy the projectile tip, in turn distributing the kinetic energy over the backing which reflects the tensile wave and captures the shattered ceramic[6]. Despite the effective penetration blocking of these armour systems, a remainder of the kinetic energy is still distributed to the wearer, often resulting in behind armour blunt trauma[7]. Furthermore, during impacts this form of armour is irreversibly damaged, compromising its structural integrity for further use. The aerospace sector utilise impact energy dissipating materials for the unique task of capture and preservation of space debris, space dust and micrometeoroids[8]. These captured projectiles contribute towards our understanding of the local environments of aerospace equipment, including that of the international space station[9]. Data from these experiments facilitate aerospace equipment design, improving the safety of astronauts and the longevity of costly aerospace equipment. Aerogels are the current industry standard for projectile capture and preservation, achieving energy dissipation through conversion of projectile kinetic energy into both mechanical and thermal energy[10]. However, the resulting temperature elevation, further enhanced by the remarkable insulating properties of aerogel[11], can cause the aerogel structure to melt[10]. Furthermore, these elevated temperatures may compromise the structure of the captured projectiles, altering its chemical composition[10, 12]. This thermal and mechanical energy, causes chemical bond breakage, rendering the aerogel irreversibly damaged post-impact. It is apparent from the aforementioned examples that a material utilising an energy dissipation mechanism that reforms following the removal of force would alleviate inherent issues seen with the industry standard materials. Additionally, specifically for the aerospace sector, energy dissipation that does not result in the conversion of kinetic to thermal energy would be beneficial.

Within the animal kingdom, proteins that offer unique mechanical properties are rife; silk fibroin displays modifiable macroscale properties in its assembled fibre form, while elastin instils elasticity in animal tissues[13]. Although there are many proteins analogous to these examples, very few researchers have tapped into these natural resources for development of materials with novel mechanical properties[14-16]; even fewer have tested these materials for real world applications outside of the biomedical sector[13]. Talin (Fig. 1a) is the epitome of a mechanical protein, mediating the connection between the actin cytoskeleton and the integrin extracellular matrix receptors, acting as a mechanosensor. Previous work determined that, through unfolding/refolding events of its thirteen four/five helical rod domains[17, 18,19, 20] when stretched within the physiologically relevant range, talin is able to maintain the average force experienced by the protein below 10 pN[18]. Furthermore, upon removal of force, refolding of the talin rod domains occur with high fidelity over numerous force cycles[18] confirming talin as a cellular shock absorber.

Here, we have engineered a recombinant form of talin, termed pGEL, which comprises three rod domains of talin, R1-R3, that are modified (with internal cysteine residues mutated to serine and

73 cysteine residues introduced at either end of the protein) for use as the monomer with which to form
74 a polymer. When exposed to force, these three domains provide a stepwise unfolding, with the wild
75 type domains exhibiting threshold unfolding forces of 20, 15 and 5 pN respectively[18]. We hypothesised
76 that, upon application of force (i.e. shear strain or impact), the three rod domains within each protein
77 monomer would unfold, dissipating energy through the endothermic process of protein unfolding[21]
78 (Fig. 1g-i).

79

80 **Fig. 1 The design concept of TSAM. a**. Cartoon representation of the protein talin, F = FERM domain, R = rod domain, DD =
81 dimerisation domain[20]. The R1-R3 domains that were engineered to form the pGEL monomer are highlighted in orange. **b.**
82 Chemical structure of the control compound **1** (Fig. S2 and S4) and the trivalent crosslinker **2** (Fig. S3-S4), **c**. pGEL in the folded
83 state, green boxes = flexible linkers with a terminal thiol containing cysteine residue, blue box = modified R1-R3 domains of
84 talin. **d.** Reaction of the pGEL monomer with compound **2** (not to scale). **e.** Hydrogel formed from the reaction of the pGEL
85 monomer (200 mg/mL) with **2**. No gelation was observed with **1**. **f.** Hypothesised structure of network formed at the
86 molecular level through the reaction of thiol containing cystine residues contained within the pGEL monomer and **2** with no
87 applied strain. **g**. pGEL in fully folded state presents length of ≈15 nm, measurements based on estimated length of R1-R3 of
88 the wild type protein in resting state[22, 23]. **h**. When exposed to strain pGEL unfolds into a linear string of helices extending to
89 ≈65 nm in length, measurements based on estimated length of R1-R3 of the wild type protein[18, 22, 24]. **i**. When exposed to
90 higher strain, pGEL unfolds fully into extended polypeptide, increasing to a length of 156 nm, measurements based on
91 estimated length of R1-R3 of the wild type protein under >25 pN[24]. The R1-R3 rod domains refold once strain is removed[24].

92

93

94   Using compounds **1** (control monovalent compound) and **2** (trivalent crosslinker) (Fig. 1b,
95 Supplementary Fig. 1-3), pGEL (Fig. 1c) was formed into a hydrogel (Fig. 1e-f) via tri-substitution of the

96   terminal cysteines with crosslinker **2** (Fig. 1d and Supplementary Fig. 4). The resulting hydrogel, which
97   we have termed TSAM (Talin Shock Absorbing Material), therefore contains monomeric units capable
98   of refolding upon removal of force, retaining its energy dissipating mechanism following any potential
99   impact events. Due to the endothermic energy dissipating mechanisms of protein unfolding[21] in TSAM,
100   the heating of the captured projectiles seen with aerogels energy dissipating mechanism would not
101   be observed, offering a solution to several of the limitations seen with current state of the art impact
102   absorption materials. The use of compound **1** supports our conclusion that compound **2** is responsible
103   for the pGEL monomer polymerisation processes and resultant material formation (Fig. 1d).

TSAM structural characterisation

105   The R1-R3 domains of talin incorporated in the pGEL monomer were confirmed to retain alpha
106   helical folding, using circular dichroism and ^{1}H-^{15}N HSQC nuclear magnetic resonance (Supplementary
107   Fig. 5-8). Following formation of TSAM, characterisation of the internal network structure was
108   conducted. Fourier Transform infrared (FT-IR) spectroscopy[25] confirmed that the helical nature of the
109   talin domains was still present in the material structure (Supplementary Fig. 9). His-tagged gold
110   immunostaining of the TSAM, imaged using transmission electron microscopy (TEM), confirmed the
111   presence of pGEL in a lattice formation, displaying pore sizes of approximately 100 nm (Fig. 2a).
112   Following this, scanning electron microscopy (SEM) revealed TSAM to contain a porous like structure
113   on the micrometre scale typical of hydrogels (Fig. 2b), with long fibres of width ≈2 µm and pores of
114   ≈10 µm. Elemental dispersive X-ray (EDX) analysis confirmed the observed fibres in the SEM images
115   consisted of sulphur and carbon (Fig. 2c), pGEL representing the only component of the xerogel
116   containing these atoms. Together these findings indicated pGEL molecules linked with crosslinker **2**
117   form a lattice on the nanometre scale, morphing into larger fibrillar like structures on the micrometre
118   scale. When handling TSAMs, high levels of extensibility were observed, presenting extension of >3-
119   fold when under tension, and returning to original size upon removal of force (Fig. 2d-e).

120

Evidence for pGEL domain unfolding in TSAM

122   Rheological characterisation of TSAMs provided strong evidence for the induced unfolding of
123   the talin domains within the material when exposed to shear strain, indicating that the energy
124   dissipating mechanisms of talin were successfully incorporated into the TSAM. Here, oscillatory shear
125   strain sweeps were conducted, whereby a sinusoidal oscillation of a pre-set shear strain was applied
126   to the TSAM at a set frequency, with the resultant shear stress measured. A total of five consecutive
127   oscillatory shear strain sweeps, with a two minute rest period between each sweep, were conducted
128   on three different TSAM samples to ensure reproducibility of results.

129   For the first applied oscillatory shear strain sweep on the TSAM, the dynamic shear storage
130   (G') and loss modulus (G"), as a product of shear strain presented a linear viscoelastic region (LVER)
131   for the full range of shear strain tested (Supplementary Fig. 10). The LVER indicates the range of shear
132   strain at which the material acts elastically[26], revealing the TSAMs as stable materials with high levels
133   of extensibility. Following this, four further oscillatory shear strain sweeps were conducted
134   (Supplementary Fig. 10-14, Fig. 2f). Owing to the unfolding and refolding kinetics intrinsic to R1-R3,
135   we hypothesised viscoelastic properties would be retained upon repeated exposure to shear strain.
136   As hypothesised, during all five oscillatory shear strain sweeps, the TSAMs presented G' > G"

137   throughout the range of shear strain tested, confirming conserved viscoelastic behaviour
138   (Supplementary Fig. 10-14). During sweeps 3-5, a positive gradient of G' occurring with increased
139   shear strain on the X-axis (Fig. 2f) was observed in place of the LVER seen with sweeps 1-2. Such an
140   observation is termed strain stiffening. Here, the peak maxima for G' occurred between 1-5% for
141   sweeps 3-5, shifting to the right and increasing in amplitude for each subsequent sweep (Fig. 2f). Strain
142   stiffening was further observed as the concomitant increase of the complex modulus (G*) (sum of G'
143   and G") with accumulated sweeps. The presence of strain stiffening both across and between sweeps
144   reveal TSAMs to present increased resistance to deformation upon repeated exposure to shear
145   strain[27]. Strain stiffening as a consequence of fibre reorganisation, such as the TSAM fibres depicted
146   in Fig. 2b, is a well-documented phenomenon occurring in hydrogels formed from biopolymers[28],
147   causing the elastic modulus to increase with strain. We propose the strain stiffening observed here
148   results from a greater number of talin domains arranged in parallel to the axis of the fibres (Fig. 2g),
149   resulting in the overall increased network rigidity observed.

150   Following the peak maxima of G' for sweeps 3-5 displayed in Fig. 2f, G' began to decrease with
151   increasing shear strain. A decrease in G' indicates a reduction in the materials rigidity. Furthermore,
152   the phase angle across each sweep (displayed in Fig. 2h), revealed a bell shaped curve, with the peak
153   amplitude of the bell increasing for each subsequent sweep. The positive slope of the phase angle in
154   Fig. 2h corresponded to the negative gradient of G' in Fig. 2f for the same respective sweep. Thus, an
155   increase in phase angle was observed simultaneously with a decrease in rigidity. A sudden increase in
156   phase angle is caused by a lag between the applied sinusoidal shear strain and the resulting shear
157   stress, occurring from a rapid increase in viscosity. Interestingly, the phase angle reached a maxima at
158   ~10-15% shear strain, with the phase angle then declining, revealing a decrease in viscosity with the
159   further increase of shear strain. When combined, the above observations are all accounted for by the
160   induction of the pGEL monomer unfolding within TSAMs (Fig. 2g). Specifically, as a result of the
161   increased network rigidity observed as strain stiffening, strain can become imparted on the fibres
162   themselves. When a maximum fibre strain is reached, mass chain unfolding of the TSAM R1-R3
163   domains occur, reducing the materials rigidity and introducing slack into the system from the
164   extension (Fig. 1g-i) of the now unfolded pGEL monomer domains. This slack registers as the
165   decreased rigidity (decrease in G') and sudden increase in phase angle. Following application of
166   increasing shear strain, the slack from unfolded TSAM R1-R3 domains is taken up, increasing the
167   tension on the fibres and as a result the materials rigidity. This is observed as the decrease in phase
168   angle (Fig. 2h) and increase in G' (Fig. 2f). Oppositely, if the material were reaching a gelation to
169   solution transition point as a consequence of internal structure breakage, the phase angle would have
170   continued to increase above 45 degrees. Upon removal of shear strain, the unfolded R1-R3 domains
171   may then refold, and the resulting TSAM displays an enhanced rigidity (higher G* at the start of the
172   next sweep) due to fibre network reorganisation. Shear stress vs. shear strain correlations corroborate
173   these results, revealing an exponential increase in shear modulus (G), a measure of rigidity, with
174   accumulated sweeps, further illustrating the strain stiffening within the TSAM (Fig. 2i). Furthermore,
175   sweeps 4 and 5 reach shear yield points, beginning to move into viscous stress as seen by the induction
176   of a slope, subsequently transitioning back into a linear gradient indicating the reoccurrence of elastic
177   behaviour. In summary, the linear elastic region at low shear strain is a result of reordering of the
178   network structure and gradual tension accumulating in the fibres, the following curve transition
179   indicates the sudden mass unfolding of talin rod domains, and subsequent linear region reports
180   elasticity reoccurring once tension is again applied to the fibres with increasing shear strain.

181

182
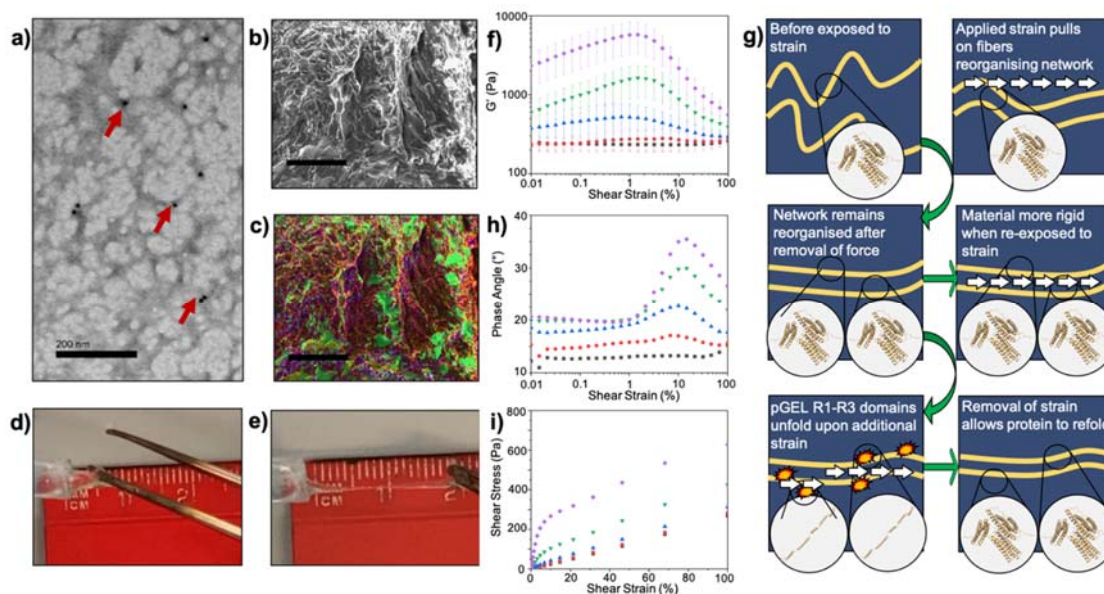
Fig. 2 The internal fibre structure of TSAM and its macroscale characterization. a. Immunogold-stained TSAM imaged with TEM showing lattice structure of connected pGEL proteins. Gold particles are observed as black dots, some of which are highlighted with red arrows (Scale bar = 200 nm). **b**. The dense fibre structure of TSAM displaying a porous network imaged with SEM on secondary electron mode (Scale bar = 50 μm). Pore sizes are on the range of a few μm. **c**. EDX analysis of SEM image in b. sulphur = yellow, carbon = red, oxygen = green, sodium = teal, phosphorus = purple. (Scale bar = 50 μm). Please note that SEM and the TEM show the overall topology of the gel, at two different resolution scales. **d**. TSAM slightly stretched. **e**. TSAM stretched to 3x its length. **f-i**. Rheological measurements of TSAM (n = 3). **f**. G' as a product of shear strain (error bars = SEM) for sweeps 1 (squares), 2 (circles), 3 (triangles), 4 (inverted triangles) and 5 (diamonds). **g**. Schematic summary of the events hypothesised to occur over 5 x repeated oscillatory sweeps. **h**. Phase angle against shear strain for sweeps 1-5 on TSAM. **i**. Shear stress against shear strain for sweeps 1-5 on TSAM.

193

To confirm that the unfolding of the talin domains within the TSAM was directly responsible for the rheological characteristics/material properties observed, a green fluorescent protein tagged-vinculin domain 1 protein (GFP-VD1) was employed. GFP-VD1 is capable of selectively binding to the unfolded state of each of the rod domains (Fig. 3a, Supplementary Fig. 15), preventing domain refolding and 'locking' the extended conformation[24]. Here the GFP-VD1 was introduced into the TSAM pre-amplitude sweep as a 2 mg/mL solution through a material swelling process. The rheological properties of these materials were then elucidated and compared to the results of analogous studies in which the same TSAM material underwent the same material swelling process in a solution of GFP or buffer only. The resulting G' and G" as a product of shear strain for the three conditions tested are summarised in Supplementary Fig. 16.

When plotted as shear stress against shear strain (Fig. 3b) the GFP and buffer controls presented the same linear trend as obtained in the first amplitude sweep for the non-treated TSAMs, indicating purely elastic behaviour. In contrast, the TSAM treated with GFP-VD1 reached a yield point between 46-68% shear strain (Fig. 3b) as a result of VD1 binding events. To further confirm the binding of GFP-VD1 to the TSAM fibres, a series of comparative fluorescence microscopy experiments were conducted. Here, fibre like structures exhibiting the same diameter as those observed in our previous SEM studies (Fig. 2b) were found to have localised GFP-VD1 (Fig. 3c-d), confirming binding. In contrast,

211   the GFP control treated TSAM fibres appeared as darker regions, with void spaces presenting higher
212   GFP concentrations (Fig. 3e-f).

213

214
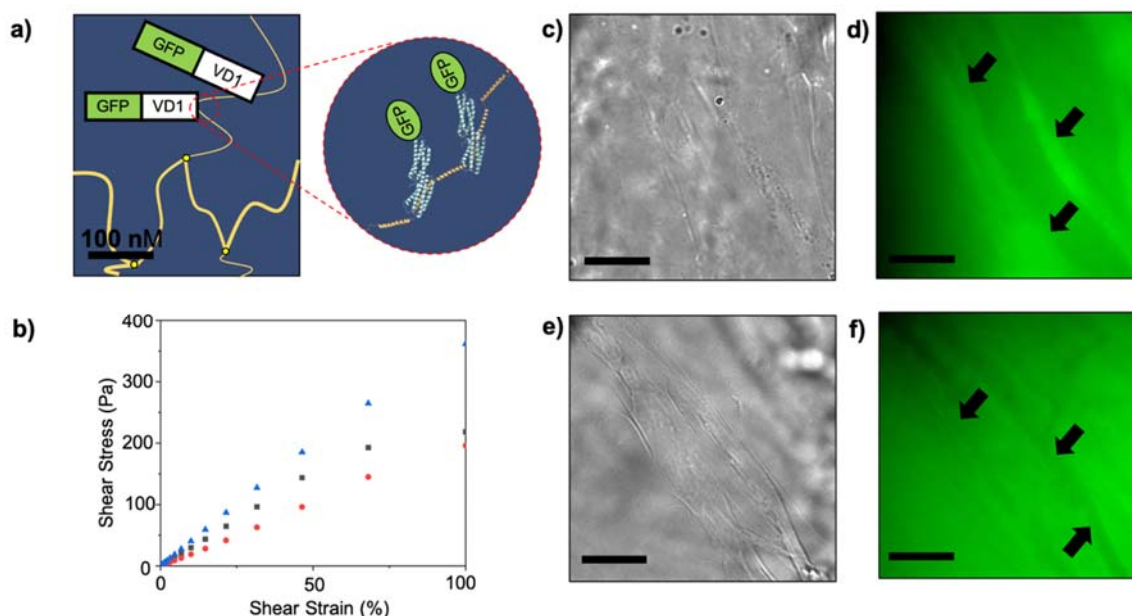
Fig. 3 Effects of GFP-VD1 on TSAM. a. Representation of GFP-VD1 binding to unfolded pGEL in TSAM fibres, with resulting cartoon protein figures created in PyMOL using VD1 PDB structure 1U6H[29]. **b**. Shear stress as a product of shear strain for buffer (blue triangles), GFP-VD1 (black squares) and GFP (red circles), showing GFP-VD1 treated TSAM reaches its yield point between 46-68% shear strain. **c**. Transmitted light image of GFP-VD1 localised to TSAM fibres (scale bar = 20 μm). **d**. Maximum projection widefield fluorescent image of c. (scale bar = 20 μm) with fibres showing localised GFP-VD1 indicated by arrows. **e**. Transmitted light image of GFP in TSAM (scale bar = 20 μm). **f**. Maximum projection widefield fluorescent image of e. showing GFP sitting in void space, with fibres this time visible as darker structures indicated by arrows (Scale bar = 20 μm).

223

TSAMs capture and preserve projectiles from supersonic impacts

225   Following the rheological evidence for TSAMs retention of talin's endothermic energy
226   dissipation mechanism, we moved on to test the performance of the TSAM as an impact absorbing
227   material, investigating TSAM performance upon supersonic projectile impact. Specifically, velocities
228   of 1.5 km/s were tested, as this is a speed relevant to the aerospace and defence industries.[30, 31] For
229   instance, particles in space impact both natural and human-made objects at speeds >1 km/s[30], while
230   muzzle velocities from firearms commonly fall between 0.4-1.0 km/s[31]. Here the TSAM, in addition to
231   a commercially available polyvinylpyrrolidone hydrogel control, were placed in the target chamber of
232   a light gas gun (LGG) and the following material properties elucidated: (1) the ability of the TSAM to
233   survive impact; (2) the ability of the TSAM to reduce the force of the projectile before impacting an
234   aluminium back plate; and (3) the ability of the TSAM to capture the projectile in a preserved state.

235   Spherical basalt particles between 20-70 μm were used as projectiles, loaded in a sabot as
236   buckshot. A schematic for this experiment is given in Fig. 4a-c. When shot at 1.5 km/s, the upper
237   ballistics limit for terrestrial based weaponry and non-meteorite impact, the control gel was destroyed
238   (Fig. 4d), with a visible hole in the tape behind the gel (Fig. 4e), and a crater of 1.33 mm in diameter

239 produced in the aluminium back plate (Fig. 4f). Therefore, this material control showed no detectable
240 impact absorption properties. However, under analogous experimental conditions, the TSAM
241 appeared mostly intact from the frontal perspective (Fig. 4g and Supplementary Fig. 17-19), with no
242 projectile permeation detected to either the supporting tape (Fig. 4h) or the aluminium backplate (Fig.
243 4i). In addition, subsequent SEM analysis identified the basalt particles embedded in the TSAM post
244 shot (Fig. 4j and Supplementary Fig. 21), confirming that the TSAM had completely absorbed the
245 impact of the basalt buckshot. An equivalent shot into aerogel revealed the majority of basalt particles
246 penetrated between 5-8 mm (Supplementary Fig. 20) indicating TSAM is competitive in performance
247 with this industrial standard, as the TSAM protected the material backing from any impact damage
248 with 5 mm depth of material. The transparency of the TSAM shown in Fig. 4c and Supplementary Fig.
249 17 is an additional desirable property, allowing for the easy removal of caught projectiles from the
250 TSAMs. To conclusively determine if TSAM also enabled preservation of the captured basalt
251 projectiles, SEM was performed on the impacted TSAM. Multiple basalt particles presenting a
252 preserved circular shape were observed in the gel (Fig. 4j-k), confirmed as basalt with EDX analysis
253 (Supplementary Fig. 21). Thus, supporting that TSAM enables projectile preservation. Moreover,
254 during one of the TSAM shots, shrapnel from the aluminium (Al 7075) burst disk (Fig. 4b) struck the
255 TSAM in combination with the basalt, as confirmed through SEM and EDX analysis (Fig. 4l and
256 Supplementary Fig. 22). Such an impact often destroys aerogel materials used as the industrial
257 standard within the aerospace industry for projectile capture, providing evidence that TSAMs are able
258 to overcome this limitation.

259
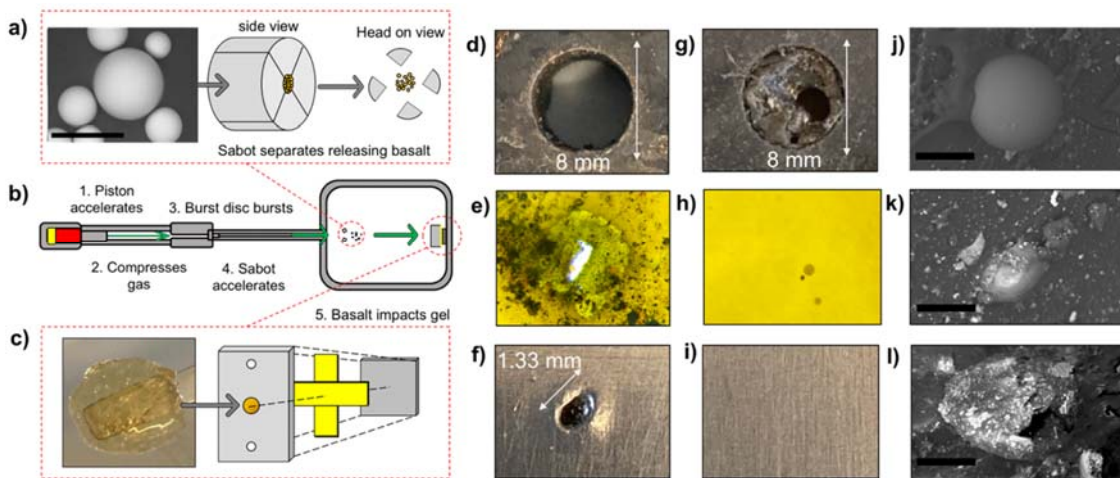
Fig. 4 Supersonic impact study on TSAM. a. SEM image of a basalt particle used as the projectile and representation of how
the basalt is loaded into a sabot and its release during a shot (scale bar = 60 µm). **b**. diagram of the light gas gun apparatus
with the key stages after the shot is triggered. **c**. image of TSAM and how it is prepared as a target. The TSAM is loaded into
a target plate constructed of steel (Blast tank exit aperture, stainless 304), with tape used to seal the back of the hole,
followed by an aluminium back plate (Al 5083). **d**-**f**. Results from control gel **d**. Destroyed control gel after basalt impact at
1.5 km/s. **e**. Hole formed in tape from basalt projectile. **f**. Crater formed in aluminium back plate. **g**-**l** results from TSAM **g**.
Mostly intact TSAM after basalt impact at 1.5 km/s. **h**. Tape with no hole, containing several caught basalt particles in the
transparent TSAM attached to its surface (Supplementary Fig. 21). **i**. Undamaged aluminium back plate. **j**. SEM image of
intact basalt particle caught by TSAM after impact at 1.5 km/s. (scale bar = 45 µm) **k**. SEM image of another basalt particle
caught by TSAM after impact at 1.5 km/s. (scale bar = 30 µm) **l**. SEM image of a fragment of the aluminium (Al 7075) burst
disc that impacted TSAM during the 1.5 km/s basalt shot (scale bar = 50 µm). Results from repeat experiments and further
images can be found in Supplementary Fig. 17-19.

272

Discussion and Outlook

In summary, we present the first example of a talin shock absorbing material (TSAM) known to literature – a SynBio material constructed from monomeric units containing force-dependent mechanical switch domains. Our previous work demonstrated that multiple talin domains in series enable talin to serve as a force buffer during large strain changes[18] and the TSAM material was designed to capture this shock absorbing property of the monomers on a macro-scale. In addition, we show that TSAMs can absorb impacts by basalt particles and larger pieces of aluminium shrapnel, providing the first example of a protein material capable of absorbing supersonic projectile impacts – with the exception of hydrogels produced from gelatine and recombinant telechelic proteins[32], which lack the intrinsic mechanosensitive properties of talin and therefore also the pGEL monomer. The difference between the TSAM and gelatine systems is further supported when considering work by Kokol and co-workers[35]. Here gelatine hydrogels demonstrate significant variations in material characteristics when compared to the TSAM systems. These variations in material characteristics will result in differences in material properties and response to impact. These results lend the TSAMs towards application within the aerospace and defence industries, e.g. as a backing for multi-layered armour where shattered ceramic capture is required, and in hypervelocity impact experiments in which the projectile needs to be preserved for further study. We believe this is as a consequence of the endothermic energy dissipating mechanism of talin[21]. This energy dissipating mechanism was confirmed using rheology, while GFP-VD1 binding experiments supported the presence of talin unfolding events within these processes. Through the reversible refolding of talin domains within TSAM following the removal of force, the material also demonstrates potential for iterative use. Finally, as talin contains thirteen helical domains, each with unique unfolding forces, these TSAMs may be tuneable by modifying the talin domains featured in the monomer unit, offering the potential for tailoring toward a diverse array of mechanical properties and resulting applications.

Methods

Protein engineering

The genes encoding pGEL, GFP-VD1 and GFP were constructed in pET151 vectors. The proteins were expressed in BL21(DE3)* *E. coli*. Protein purification was achieved using HisTrap HP columns (Cytiva) for His-tag based affinity chromatography using an AKTA Start protein purification system (Cytiva). Following purification, proteins were dialysed in phosphate buffer (20 mM sodium phosphate, pH 7.4, 50 mM NaCl).

TSAM preparation

Here TCEP (tris(2-carboxyethyl)phosphine) is used as a reducing agent. A 30:1 ratio of TCEP:cysteine was slowly added to a solution of pGEL (200 mg/mL) in phosphate buffer (pH 7.4). After one hour, the pGEL solution was run through PD10 desalting columns (Cytiva) twice to ensure TCEP removal. Immediately following the desalting step, the pGEL solution was concentrated to the desired concentration using 30 kDa MWCO concentrators (SigmaAldrich). The TSAM was then formed through the addition of crosslinker **2** at 1:1 maleimide:thiol molar ratio, which is equivalent to a 2:3 crosslinker **2**:pGEL monomer molar ratio. The TSAM was left to set at 4°C overnight.

Scanning electron microscopy

The TSAM sample was placed into a petri dish and left at 37°C until the material had completely desiccated, producing a xerogel. This xerogel was then placed on a carbon tab mounted onto an aluminium stub. Imaging was achieved using a Hitachi S-3400N scanning electron microscope with elemental dispersive X-ray analysis and analysed using Oxford instruments AZtec software.

Immuno-gold staining and transmission electron microscopy

A 2 µL of sample was applied to carbon/formvar 400 mesh gold grids (Agar Scientific) and allowed to settle on the grid for 5 minutes. The sample was then fixed in 2% formaldehyde and 0.5% glutaraldehyde in 100 mM sodium cacodylate buffer pH 7.2 (CAB) for 15 minutes at room temperature. Samples were washed 2 x 5 minutes in CAB and 2 x 5 minutes in 20 mM Tris, 500 mM NaCl, 0.1% BSA and 0.5% Tween 20 (TBST). Grids were blocked in 2% BSA in TBST for 30 minutes and then moved into a 20 µl drop of anti-His tag primary antibody (Sigma) diluted 1:100. Grids were washed 6 x 2 minutes in drops of TBST before incubation in Goat anti-mouse IgG conjugated to 5 nm gold particles (British Biocell International) diluted 1:50 for 30 minutes. Grids were washed for 6 x 2 minutes in TBST and 6 x 2 minutes in distilled water. Negative controls were performed as above but primary antibody was replaced with TBST. Samples were then air dried and negative stained in 2% aqueous uranyl acetate. Samples were viewed using a Jeol 1230 Transmission electron microscope at 80 kV and images were recorded on a Gatan OneView 16 MP digital camera.

Rheological measurements

Rheological measurements were performed on an Anton Parr modular compact rheometer (MCR302). All measurements were performed at 298 K using a PP20 parallel plate. Oscillatory amplitude experiments maintained a frequency of 10 rad/sec and were performed with an amplitude of oscillation range of 0.01-100%. A 2 minute rest time was set between each amplitude sweep, with a total of five sweeps performed on each TSAM. For the GFP-VD1, GFP and buffer swelled experiments, the TSAM was left in 2 mg/mL of the respective solution overnight before rheological measurements were performed. For the GFP-VD1 experiments, TSAMs were swelled with GFP, GFP-VD1 or buffer by being placed in the respective solution overnight at 4°C.

Fluorescence microscopy

Following rheology experiments, the resulting GFP and GFP-VD1 swelled TSAMs were washed overnight at 4°C in solution of buffer to reduce background fluorescence from unbound protein. GFP-VD1 and GFP treated samples of TSAM from the rheology experiments were visualised using an Olympus IX71 microscope employing a 1.6x magnification Optovar in combination with a PlanApo 100x OTIRFM-SP 1.49 NA lens mounted on a PIFOC z-axis focus drive (Physik Instrumente, Karlsruhe, Germany), and illuminated using LED light sources (Cairn Research Ltd, Faversham, UK) with DC/ET350/50x excitation, ET Quad Sedat dichroic, and DC/457/50m emission filters (Chroma, Bellows Falls, VT). Samples were visualised using a QuantEM (Photometrics) EMCCD camera, and the system was controlled with Metamorph software (Molecular Devices). Each 3D-maximum projection of volume data was calculated from 31 z-plane images and the best 6 were chosen, each 0.2 µm apart, and analysed using MetaMorph software.

Light gas gun experiments

The impact experiments were carried out using the Light Gas Gun (LGG) facility at the University of Kent, Canterbury. The LGG is capable of accelerating projectiles smaller than 3.5 mm to speeds up to

356 7 km/s[33, 34]. The TSAM or control target (8 mm wide and 5 mm thick, chosen based on sample holder
357 size) was set in a blast tank exit aperture (BTEA) with a circular, 8 mm diameter aperture, sealed with
358 tape, with an aluminium (5083) back plate placed behind. Multiple 20-70 µm basalt particles were
359 loaded into a single sabot utilising the "buckshot" method and were fired at roughly 1.5 km/s, with
360 the speeds recorded via the BTEA - Muzzle laser method as described by Burchell et al.[33]. The target
361 was removed prior to the air flushing procedure to reduce gun contamination of the TSAM. The
362 combination of the BTEA and target mount into a single device, allowed for minimal spreading of the
363 buckshot projectile, increasing the chance of direct impact onto the TSAM, and maximized the BTEA-
364 muzzle separation. Discussion of talin unfolding rates is provided within the Supplementary
365 information.

366 **Aerogel experiments**

367 For comparison to the industry standard material, a light gas gun shot on aerogel was performed. The
368 block of aerogel displayed an initial manufacturing density 0.092 g/cc and measured 30 x 30 x 20 mm.
369 Prior to setup the aerogel was baked overnight to remove any built up moisture in the block and
370 reweighed. The post baking density was found to be 0.09 +/- 0.01 g/cc. The block was positioned in
371 the Blast tank of the LGG and backed with an AL target plate (see Supplementary Figure 20a). The
372 projectile was prepared in exactly the same way as the TSAM and control gel shots, fired at
373 approximately 1.5 km/s. The projectile consisted of a 0.170 sabot with an Internal diameter bore of
374 0.8 mm loaded with basalt sphere of sizes 25-70 µm. Microscopy images were captured using a Leica
375 PLANAPO 1.0x microscope and images were processed using Leica Application Suite X (version
376 3.7.5.24914).

377

Acknowledgements

385

References

387 1. Qiao, P.Z., Yang, M.J. & Bobaru, F. Impact mechanics and high-energy absorbing materials: Review.
388   *Journal of Aerospace Engineering* **21**, 235-248 (2008).
389 2. Dyatkin, B. US hypersonics initiatives require accelerated efforts of the materials research
390   community. *Mrs Bulletin* **46**, 201-203 (2021).
391 3. Viana, J.C. Polymeric materials for impact and energy dissipation. *Plastics Rubber and Composites*
392   **35**, 260-267 (2006).
393 4. Park, J.L., Chi, Y.S., Hahn, M.H. & Kang, T.J. Kinetic Dissipation in Ballistic Tests of Soft Body Armors.
394   *Experimental Mechanics* **52**, 1239-1250 (2012).

395   5. Fejdys, M., Kosla, K., Kucharska-Jastrzabek, A. & Landwijt, M. Influence of ceramic properties on
396   the ballistic performance of the hybrid ceramic-multi-layered UHMWPE composite armour.
397   *Journal of the Australian Ceramic Society* **57**, 149-161 (2021).
398   6. Reis, R.H.M. et al. Ballistic Performance of Guaruman Fiber Composites in Multilayered Armor
399   System and as Single Target. *Polymers* **13** (2021).
400   7. Wen, Y.K., Xu, C., Wang, S. & Batra, R.C. Analysis of behind the armor ballistic trauma. *Journal of*
401   *the Mechanical Behavior of Biomedical Materials* **45**, 11-21 (2015).
402   8. Kearsley, A.T. How laboratory hypervelocity impact experiments have helped us to understand
403   comet dust samples: a brief review. *14th Hypervelocity Impact Symposium (Hvis 2017)* **204**, 43-50
404   (2017).
405   9. Woignier, T., Duffours, L., Colombel, P. & Durin, C. Aerogels Materials as Space Debris Collectors.
406   *Advances in Materials Science and Engineering* **2013**, 484153 (2013).
407 10. Jones, S.M., Anderson, M.S., Dominguez, G. & Tsapin, A. Thermal calibrations of hypervelocity
408   capture in aerogel using magnetic iron oxide particles. *Icarus* **226**, 1-9 (2013).
409 11. Alwin, S. & Shajan, X.S. Aerogels: promising nanostructured materials for energy conversion and
410   storage applications. *Materials for Renewable and Sustainable Energy* **9, 7** (2020).
411 12. Bheekhun, N., Abu Talib, A. & Hassan, M.R. Aerogels in Aerospace: An Overview. *Advances in*
412   *Materials Science and Engineering* **2013**, 406065 (2013).
413 13. Kan, A. & Joshi, N.S. Towards the directed evolution of protein materials. *Mrs Communications* **9**,
414   441-455 (2019).
415 14. Wu, J.H. et al. Rationally designed synthetic protein hydrogels with predictable mechanical
416   properties. *Nature Communications* **9**, 620 (2018).
417 15. Fang, J. et al. Forced protein unfolding leads to highly elastic and tough protein hydrogels. *Nature*
418   *Communications* **4**, 2974 (2013).
419 16. Zhu, F.B. et al. 3D-Printed Ultratough Hydrogel Structures with Titin-like Domains. *Acs Applied*
420   *Materials & Interfaces* **9**, 11363-11367 (2017).
421 17. Bate, N. et al. Talin Contains A C-Terminal Calpain2 Cleavage Site Important In Focal Adhesion
422   Dynamics. *Plos One* **7**, e34461 (2012).
423 18. Yao, M.X. et al. The mechanical response of talin. *Nature Communications* **7**, 11966 (2016).
424 19. Funtan, S., Michael, P. & Binder, W.H. Synthesis and Mechanochemical Activity of Peptide-Based
425   Cu(I) Bis(N-heterocyclic carbene) Complexes. *Biomimetics* **4**, 24 (2019).
426 20. Goult, B.T. et al. RIAM and Vinculin Binding to Talin Are Mutually Exclusive and Regulate Adhesion
427   Assembly and Turnover. *Journal of Biological Chemistry* **288**, 8238-8249 (2013).
428 21. Schon, A., Clarkson, B.R., Jaime, M. & Freire, E. Temperature stability of proteins: Analysis of
429   irreversible denaturation using isothermal calorimetry. *Proteins-Structure Function and*
430   *Bioinformatics* **85**, 2009-2016 (2017).
431 22. Barnett, S.F.H. & Goult, B.T. The MeshCODE to scale – Visualising synaptic binary information.
432   *bioRxiv*, 2022.2006.2016.496395 (2022).

433 23. Dedden, D. et al. The Architecture of Talin1 Reveals an Autoinhibition Mechanism. *Cell* **179**, 120-
434   131 (2019).
435 24. Yao, M.X. et al. Mechanical activation of vinculin binding to talin locks talin in an unfolded
436   conformation. *Scientific Reports* **4**, 4610 (2014).
437 25. Jackson, M. & Mantsch, H.H. THE USE AND MISUSE OF FTIR SPECTROSCOPY IN THE
438   DETERMINATION OF PROTEIN-STRUCTURE. *Critical Reviews in Biochemistry and Molecular Biology*
439   **30**, 95-120 (1995).
440 26. Öhrlund, Å., Evaluation of Rheometry Amplitude Sweep Cross-Over Point as an Index of Flexibility
441   for HA Fillers. *Journal of Cosmetics, Dermatological Sciences and Applications* **8**, 47-54 (2018).

442 27. Kulkarni, V.S. & Shaw, C. in Essential Chemistry for Formulators of Semisolid and Liquid Dosages.
443   (eds. V.S. Kulkarni & C. Shaw) 145-182 (Academic Press, Boston; 2016).
444 28. Wen, Q. & Janmey, P.A. Polymer physics of the cytoskeleton. *Current Opinion in Solid State &*
445   *Materials Science* **15**, 177-182 (2011).
446 29. Fillingham, I. et al. A vinculin binding domain from the talin rod unfolds to form a complex with
447   the vinculin head. *Structure* **13**, 65-74 (2005).
448 30. Williamsen, J., Pechkis, D., Balakrishnan, A. & Ouelette, S. Characterizing the Orbital Debris
449   Environment Using Satellite Perturbation Anomaly Data. First International Orbital Debris
450   Conference. 9-12 December. Lunar and Planetary Institute: Sugar Land, Texas (2019).
451 31. Couldrick, C. in Advances in Military Textiles and Personal Equipment. (ed. E. Sparks) 196-212
452   (Woodhead Publishing, 2012).
453 32. Veysset, D. et al. High-velocity micro-particle impact on gelatin and synthetic hydrogel. *Journal of*
454   *the Mechanical Behavior of Biomedical Materials* **86**, 71-76 (2018).
455 33. Burchell, M.J., Cole, M.J., McDonnell, J.A.M. & Zarnecki, J.C. Hypervelocity impact studies using
456   the 2 MV Van de Graaff accelerator and two-stage light gas gun of the University of Kent at
457   Canterbury. *Measurement Science and Technology* **10**, 41-50 (1999).
458 34. Hibbert, R., Cole, M.J., Price, M.C. & Burchell, M.J. The Hypervelocity Impact Facility at the
459   University of Kent: Recent Upgrades and Specialized Capabilities. *14th Hypervelocity Impact*
460   *Symposium (Hvis 2017)* **204**, 208-214 (2017).
461 35. Kokol, V., Pottathara, Y. B., Mihelčič, M., & Perše, L. S. Rheological properties of gelatine hydrogels
462   affected by flow- and horizontally-induced cooling rates during 3D cryo-printing. *Colloids and*
463   *Surfaces A: Physicochemical and Engineering Aspects*, ***616***, 126356 (2021).

464

465

466